Medical Image Analysis 13 (2009) 405–418

Contents lists available at ScienceDirect

Medical Image Analysis

journal homepage: www.elsevier.com/locate/media

# Comparison of regularization methods for human cardiac diffusion tensor MRI

Carole Frindel *, Marc Robini, Pierre Croisille, Yue-Min Zhu

*CREATIS-LRMN, CNRS UMR 5220, INSERM U630, INSA of Lyon and University of Lyon1, 69621 Villeurbanne Cedex, France*

A R T I C L E   I N F O

*Article history:*
Received 8 March 2008
Received in revised form 8 January 2009
Accepted 9 January 2009
Available online 20 January 2009

*PACS:*
87.59

*Keywords:*
Diffusion tensor MRI
Cardiac imaging
Diffusion weighted image regularization
Tensor field regularization
Tractography

A B S T R A C T

Diffusion tensor MRI (DT-MRI) is an imaging technique that is gaining importance in clinical applications. However, there is very little work concerning the human heart. When applying DT-MRI to in vivo human hearts, the data have to be acquired rapidly to minimize artefacts due to cardiac and respiratory motion and to improve patient comfort, often at the expense of image quality. This results in diffusion weighted (DW) images corrupted by noise, which can have a significant impact on the shape and orientation of tensors and leads to diffusion tensor (DT) datasets that are not suitable for fibre tracking. This paper compares regularization approaches that operate either on diffusion weighted images or on diffusion tensors. Experiments on synthetic data show that, for high signal-to-noise ratio (SNR), the methods operating on DW images produce the best results; they substantially reduce noise error propagation throughout the diffusion calculations. However, when the SNR is low, Rician Cholesky and Log-Euclidean DT regularization methods handle the bias introduced by Rician noise and ensure symmetry and positive definiteness of the tensors. Results based on a set of sixteen ex vivo human hearts show that the different regularization methods tend to provide equivalent results.



## 1. Introduction

Diffusion tensor magnetic resonance imaging (DT-MRI) – which measures the diffusion of water molecules along various directions within tissues – provides unique and biologically relevant information without invasion. This information includes parameters that help to characterize physical properties of tissue constituents, tissue microstructure and its architectural organization. The construction of the diffusion tensor distribution requires the acquisition of a set of diffusion-weighted (DW) images associated with diffusion sensitization along $N$ non-collinear gradient directions ($N \geqslant 6$). More specifically, it is possible to estimate a $3 \times 3$ symmetric positive definite matrix $T$ (the diffusion tensor) at each location that characterizes the diffusion process. The diffusion tensor is related to the DW measurements $\mathbf{S} : S_i \ (i = 1, \ldots, N)$ according to the Stejskal-Tanner diffusion equations: $S_i = S_0 \exp(-cg_i T g_i^t)$, where $g_i$ is the diffusion encoding gradient direction associated to $S_i$, $S_0$ is the MR measurement without diffusion sensitization, and the constant $c$ is the diffusion weighting factor.

DT-MRI is particularly subject to noise for two reasons. First, since multiple DW images are needed, each individual image has to be acquired relatively quickly, thus reducing the signal-to-noise ratio (SNR). Second, DT-MRI measures physical properties (water diffusion) that require careful treatment of the noise. Therefore, image processing techniques to remove noise in the DW images or in the estimated tensor field are important, especially to perform streamlining tractography. The methods investigated here apply either to raw data (DW images) or to diffusion tensor fields. We do not consider the methods that apply to principal direction fields since we are interested in working as closely as possible to DW images to prevent noise propagation.

In DW image regularization, the denoising process is either applied to each DW image independently (e.g. Parker et al., 2000 and Basu et al., 2006) or takes coupling between the different DW images into account to synchronize their evolution (e.g. Vemuri et al., 2001 and McGraw et al., 2004). The common idea is to introduce prior information about the solution in order to smooth the DW images while preserving relevant details. One generally uses a non-quadratic regularization term on the intensity gradient modulus. During this process, large gradients are preserved while small gradients are smoothed, which allows preservation of both edges and local coherence of DW-images. A common idea to restore multivalued images is to use classical scalar anisotropic diffusion on each $S_i$ of the set of DW images $\mathbf{S}$ (Parker et al., 2000). However, this scheme is criticizable since each DW image $S_i$ evolves independently with different smoothing geometries. To take into account coupling between the different DW images, Vemuri et al. (2001) proposed a weighted TV-norm regularization method to smooth the multivalued image $\mathbf{S}$: the diffusion corresponds to scalar TV-norm regularization (applied independently on each $S_i$) weighted by a coupling term, which is the same for all $S_i$ in order to ensure their synchronized evolution.

* Corresponding author. Tel.: +33 4 72 43 87 86; fax: +33 4 72 43 85 26.
*E-mail addresses:* carole.frindel@creatis.insa-lyon.fr (C. Frindel), marc.robini@creatis.insa-lyon.fr (M. Robini).

1361-8415/$ - see front matter © 2009 Elsevier B.V. All rights reserved.
doi:10.1016/j.media.2009.01.002

Another class of regularization methods operates directly on tensor fields. However, tensor computing is difficult due to some limitations of standard Euclidean calculus. Diffusion tensors do not form a vector space since they are symmetric positive definite matrices whose space is restricted to a convex half cone (Pennec et al., 2006). Therefore, special care must be taken in order not to reach the boundaries of the non-linear tensor space, which leads to null or negative eigenvalues. To overcome these limitations, Wang et al. (2004) proposed to parameterize the diffusion tensor $T$ by its Cholesky factor $F$; smoothing the tensor's Cholesky factor in the Euclidean framework insures that $T = FF^t$ is positive, but definiteness is not insured since null eigenvalues are still possible. Pennec et al. (2006) recently developed another approach to solve the definiteness problem: the tensor space is replaced by a Riemannian manifold where $3 \times 3$ matrices with null or negative eigenvalues are at infinite distance from any tensor. It involves a new metric family, the so-called Log-Euclidean metrics, which amounts to classical Euclidean computations in the domain of matrix logarithms. This method takes into account prior knowledge about the diffusion tensor itself – like symmetry and positive definiteness – and prevents the tensor swelling effect that is observed when using the Euclidean framework. Note that there exists other matrix-valued image smoothing techniques that are not covered in this work. We refer the interested reader to a survey by Weickert and Brox (2002).

The aim of this work is to focus on the application of regularization methods to human cardiac DT-MRI datasets. This kind of study has never been conducted before, although it is of great interest to better comprehend the impact of DT-MRI in cardiological diagnosis. In fact, to apply DT-MRI to the in vivo heart, the data have to be acquired rapidly to minimize artefacts due to cardiac and respiratory motions, often at the expense of image quality. This results in DT-MRI datasets with very low SNR (much lower than in neurology), that are not suitable for fibre tracking or for building a statistical heart model (Peyrat et al., 2007). Therefore, there is a need of reliable algorithms to improve image and tensor fields. We investigate the characteristics and limitations of six regularization methods: three operating on DW images (Basu et al., 2006; Parker et al., 2000; Vemuri et al., 2001) and three operating on diffusion tensor fields (Tschumperle et al., 2001; Fillard et al., 2007; Wang et al., 2004). For each of them, we make two different noise assumptions: Gaussian and Rician. The real nature of the noise in MR magnitude images is known to be Rician (Henkelman, 1985). However, the Rician distribution can be approximated by a Gaussian distribution when the SNR is sufficiently high (Gudbjartsson and Patz, 1995; Sijbers et al., 1998).

In order to evaluate the solutions produced by these methods, we focused on the following three representations of the DT-MRI processing pipeline: tensors, parametric maps and fibres. Evaluations were performed using different metrics: the Frobenius norm for tensors, the $\ell_1$-norm for parametric maps and for the helix angle and the sheet angle for fibres, which are standards in cardiology to characterize the heart architecture.

The paper is organized as follows. Section 2 formulates the essential aspects of regularization methods and their underlying assumptions. Section 3 presents our framework for comparing the methods. The results on synthetic and real data are exposed in Section 4. Finally, conclusions are given in Section 5.

## 2. Regularization methods

### 2.1. Regularization operating on DW images

Our goal here is to denoise the DW volumes obtained by stacking up the DW images. We start from the simple model:

$$\widetilde{S}_i = S_i + \eta, \quad i \in \{1, \ldots, N\} \tag{1}$$

where $\widetilde{S}_i$ and $S_i \in L^2(\Omega)$, respectively stand for the observed data and the ideal noiseless DW volume to be reconstructed ($\Omega$ is an open-bounded set in $\mathbb{R}^3$) and where $\eta$ is the noise component.

#### 2.1.1. Scalar regularization

In the scalar regularization framework, $S_i$ is estimated by minimizing a cost functional $U : L^2(\Omega) \to \mathbb{R}$ of the form:

$$U(S_i) = H(S_i) + \lambda\Phi(S_i) \tag{2}$$

where $H$ measures fidelity to the data, the regularization term $\Phi$ measures how well its argument matches our a priori knowledge about $S_i$, and the hyper-parameter $\lambda$ balances the two terms.

We consider the anisotropic diffusion regularization term originally proposed by Perona and Malik (1990), which has been shown in You et al. (1996) to be the gradient descent flow for the following variational integral:

$$\Phi(S_i) = \int_\Omega \phi(\|\nabla S_i\|) d\Omega \tag{3}$$

where $\|\nabla S_i\|$ is the modulus of the gradient of $S_i$. The function $\phi : \mathbb{R} \to \mathbb{R}$ is chosen to allow edge-preservation (Charbonnier et al., 1997). In our experiments, we use

$$\phi(t) = 2(1 + t^2/\delta^2)^{1/2} \tag{4}$$

where $\delta$ is a fixed gradient threshold.

If the noise $\eta$ is assumed to follow a Gaussian distribution, maximum log-likelihood estimation reduces to least-squares estimation, which amounts to minimize

$$H_{\text{Gauss}}(S_i) = \int_\Omega \|S_i - \widetilde{S}_i\|^2 \, d\Omega. \tag{5}$$

If the noise $\eta$ is assumed to follow a Rician distribution, the probability density function of the pointwise observed signal $\widetilde{S}_i(x)$ knowing the pointwise expected signal $S_i(x)$ is given by:

$$\mathrm{P}\left(\widetilde{S}_i(x) = \alpha_0 | S_i(x) = \alpha\right) = \frac{\alpha_0}{\sigma^2} \exp\left(-\frac{\alpha_0^2 + \alpha^2}{2\sigma^2}\right) I_0\left(\frac{\alpha\alpha_0}{\sigma^2}\right) \tag{6}$$

where $I_0$ is the modified 0th order Bessel function of the first kind and $\sigma^2$ is the noise variance (Basu et al., 2006).

Using the Rician distribution as the likelihood term and assuming independent noise, the maximum log-likelihood estimation amounts to minimize:

$$H_{\text{Rice}}(S_i) = -\int_\Omega \log \mathrm{P}(\widetilde{S}_i | S_i) \, d\Omega. \tag{7}$$

#### 2.1.2. Multivalued regularization

In the multivalued regularization framework, the raw vector valued image $\mathbf{S} \in (L^2(\Omega))^N$ is estimated by minimizing a cost functional $U : (L^2(\Omega))^N \to \mathbb{R}$ of the form:

$$U(\mathbf{S}) = H(\mathbf{S}) + \lambda\Phi(\mathbf{S}) \tag{8}$$

where $H$ is the data fidelity term and the smoothing parameter $\lambda$ balances the effect of $H$ with the prior term $\Phi$.

In order to regularize the DW images ($N \geqslant 6$), Vemuri et al. (2001) consider a weighted TV-norm regularization term. This variational formulation is the vector-valued matching piece of the total variation formalism, largely used to regularize scalar images:

$$\Phi(\mathbf{S}) = \int_\Omega g(\lambda_{\max}, \lambda_{\min}) \sum_{i=1}^N \|\nabla S_i\| \, d\Omega \tag{9}$$

where $\|\nabla S_i\|$ is the modulus of the gradient of $S_i$. Note that this regularization term corresponds to the $\phi$-functional framework with $\phi(t) = t$.

This term involves a selective smoothness constraint on the solution achieved by the term $g(\lambda_{\max}, \lambda_{\min}) = 1/[1 + \{(\lambda_{\max} - \lambda_{\min})/\lambda_{\max}\}^2]$, where $\lambda_{\max}$ and $\lambda_{\min}$ respectively stand for the largest and smallest eigenvalues of the diffusion tensor computed from the initial data $\tilde{\mathbf{S}}$. This function has small value as the relative difference in $\lambda_{\max}$ and $\lambda_{\min}$ becomes large (smoothing is stopped). Indeed, in DT-MRI, we are interested in the anisotropy of the tensors which translates the reliability for the fibre tract mapping.

Vemuri et al. (2001) only consider the case where the noise $\eta$ is assumed to follow a Gaussian distribution, so that the data fidelity term corresponds to:

$$H_{\text{Gauss}}(\mathbf{S}) = \int_\Omega \sum_{i=1}^{N} \|S_i - \widetilde{S}_i\|^2 \, d\Omega. \tag{10}$$

### 2.1.3. PDE methods for minimization

Finding the functions $S_i$ and $\mathbf{S}$ that minimize cost functionals (2) and (8) is not an easy task. Nevertheless, the Euler-Lagrange equations (with Neumann boundary conditions) associated to them give necessary conditions that must be verified by $S_i$ and $\mathbf{S}$ to be a local minimum of their associated cost functional.

*2.1.3.1. Scalar regularization.* The unique solution of (2) satisifies the following Euler-Lagrange equation:

$$\frac{\partial H(S_i)}{\partial S_i} + \lambda \frac{\partial \Phi(S_i)}{\partial S_i} = 0 \tag{11}$$

where

$$\begin{aligned} \frac{\partial H_{\text{Gauss}}(S_i)}{\partial S_i} &= \nabla H_{\text{Gauss}}(S_i) = 2(S_i - \widetilde{S}_i) \\ \frac{\partial H_{\text{Rice}}(S_i)}{\partial S_i} &= \nabla H_{\text{Rice}}(S_i) = -\frac{S_i}{\sigma^2} + \frac{\widetilde{S}_i}{\sigma^2} \frac{I_1}{I_0}\left(\frac{S_i \widetilde{S}_i}{\sigma^2}\right) \\ \frac{\partial \Phi(S_i)}{\partial S_i} &= \nabla \Phi(S_i) = -\text{div}(\phi'(\|\nabla S_i\|) \; \|\nabla S_i\|) \end{aligned} \tag{12}$$

with $\phi'(t) = (1 + t^2/\delta^2)^{-1/2}$ and $I_1$ being the modified $1^{st}$ order Bessel function of the first kind.

To avoid the direct and difficult resolution of these PDE, we use the standard gradient descent technique (Rudin et al., 1992; Deriche and Faugeras, 1996). Starting from an initial function $S_i^0$ and following the opposite direction of the gradient of $U$ leads to a local minimizer of $U$. If the $l$-th iterate is $S_i^l$, the evolution of gradient descent is simply:

$$S_i^{l+1} = S_i^l - \alpha^l \nabla U(S_i) \tag{13}$$

where $\nabla U(S_i) = \nabla H(S_i) + \lambda \nabla \Phi(S_i)$ is the gradient of $U$, $\alpha^l$ is the gradient descent step associated with the $l$-th iterate that satisfies Wolfe's conditions (Wolfe, 1969; Wolfe, 1971). We take the initial function $S_i^0$ to be the noisy DW volume.

*2.1.3.2. Multivalued regularization.* The unique solution of (8) satisifies the following Euler-Lagrange equations:

$$\frac{\partial H(\mathbf{S})}{\partial S_i} + \lambda \frac{\partial \Phi(\mathbf{S})}{\partial S_i} = 0 \;\; i = \{1, \ldots, N\} \tag{14}$$

where

$$\begin{aligned} \frac{\partial H_{\text{Gauss}}(\mathbf{S})}{\partial S_i} &= \nabla H_{\text{Gauss}}(\mathbf{S}) = 2(S_i - \widetilde{S}_i) \;\; i = \{1, \ldots, N\} \\ \frac{\partial \Phi(\mathbf{S})}{\partial S_i} &= \nabla \Phi(\mathbf{S}) = -\text{div}\left(\frac{g(\lambda_{\max}, \lambda_{\min}) \nabla S_i}{\|\nabla S_i\|}\right) \;\; i = \{1, \ldots, N\} \end{aligned} \tag{15}$$

The gradient descent associated to the above minimization is given by:

$$S_i^{l+1} = S_i^l - \alpha^l \nabla U(\mathbf{S}) \quad i = \{1, \ldots, N\} \tag{16}$$

where $\nabla U(\mathbf{S}) = \nabla H(\mathbf{S}) + \lambda \nabla \Phi(\mathbf{S})$ is the gradient of $U$. As for the scalar case, the initial function $S_i^0$ is the noisy DW volume.

## 2.2. Tensor field regularization

According to the Stejskal-Tanner diffusion equations, the DW measurements can be modeled as:

$$\widetilde{S}_i = S_i(T) + \eta, \quad i \in \{1, \ldots, N\} \tag{17}$$

where

$$S_i(T) := S_0 \exp(-c g_i T g_i^{\text{t}}), \tag{18}$$

$T : \Omega \subset \mathbb{R}^3 \to \mathrm{M}_3(\mathbb{R})$ is the diffusion tensor field to be reconstructed, $\eta$ models the noise and $\mathrm{M}_3(\mathbb{R})$ is the set of real $3 \times 3$ matrices (again, $\Omega$ is an open-bounded subset of $\mathbb{R}^3$).

The joint estimation and regularization of diffusion tensor fields can be tackled by minimizing a cost functional $V$ similar to the one used for DW volumes:

$$V(G) = H(G) + \lambda \Phi(G) \tag{19}$$

where $H$ is the data fidelity term, $\Phi$ is the regularization term, and $\lambda$ is a normalization factor between the two terms. $G$ stands for the tensor field distribution or the distribution of a particular feature that parametrizes the tensor (matrix logarithm, Cholesky factor, etc).

The regularization term is similar to the anisotropic diffusion term applied on DW images:

$$\Phi(G) = \int_\Omega \phi(\|\nabla G\|) \; d\Omega \tag{20}$$

where $\|\nabla G(x)\| = \sqrt{\sum_{i,j} \|\nabla G_{i,j}\|^2}$ is the Frobenius norm of the Jacobian matrix. The function $\phi$ has the same characteristics as those required for DW volume regularization. We shall use the same $\phi$-function as in (4).

### 2.2.1. Euclidean regularization

The classical approach works on tensor fields in the Euclidean framework (e.g. Tschumperle et al., 2001). Let $T_1$ and $T_2$ be two tensors. An example of Euclidean structure is given by the so-called Frobenius metric: $d_{\text{E}}(T_1, T_2) = (\text{Trace}((T_1 - T_2)^2))^{1/2}$. So $G$ in (19) and (20) can be substituted by $T$.

In this situation, the data fidelity terms for Gaussian and Rician noise models are respectively defined by:

$$H_{\text{Gauss}}(T) = \sum_{i=1}^{N} \int_\Omega (S_i(T) - \hat{S}_i)^2 \; d\Omega. \tag{21}$$

$$H_{\text{Rice}}(T) = -\sum_{i=1}^{N} \int_\Omega \log \mathrm{P}(\hat{S}_i | S_i(T)) \; d\Omega. \tag{22}$$

### 2.2.2. Cholesky regularization

Wang et al. (2004) based their regularization method on Cholesky factor that parameterize the tensor and belong to a vector space. In this case, positivity and symmetry are ensured by Cholesky factorization: $\forall x \in \Omega$, $T(x) = F(x)F(x)^{\text{t}}$ where $F(x)$ is a lower triangular matrix. Therefore $G$ in (20)–(22) is substituted by $F$ (the distribution of Cholesky factors) and $S_i(F) = S_0 \exp(-c g_i F F^{\text{t}} g_i^{\text{t}})$. Here, the diffusion tensor field $T$ to be reconstructed is a mapping from $\Omega \subset \mathbb{R}^3$ to the set of $3 \times 3$ symmetric positive semi-definite matrices.

### 2.2.3. Log-Euclidean regularization

Pennec et al. (2006) decribe a framework for performing anisotropic diffusion on tensors while preserving symmetry and positive definiteness. They prove that there exists a one-to-one correspondence between symmetric matrices and tensors: the logarithm of a tensor is a symmetric matrix and the exponential of any symmetric matrix yields a tensor. Based on these specific properties, a novel Riemannian structure can be defined. Let $L_1$ and $L_2$ be the logarithm associated with two tensors $T_1$ and $T_2$, the novel Riemannian structure is given by the so-called Log-Euclidean metric: $d_{\mathrm{L}}(T_1, T_2) = (\mathrm{Trace}((L_1 - L_2)^2))^{1/2}$. The processing of tensors in the Log-Euclidean framework is simply Euclidean in the logarithmic domain. After carrying out the computations on the tensor logarithms, the results are mapped back to the tensor space with the matrix exponential. Therefore, $G$ in (20)–(22) is substituted by $L$ (the distribution of tensor logarithms) and $S_i(L) = S_0 \exp(-cg_i \exp(L) g_i^{\mathrm{t}})$. Here, the diffusion tensor field $T$ to be reconstructed is a mapping from $\Omega \subset \mathbb{R}^3$ to the set of $3 \times 3$ symmetric positive definite matrices.

### 2.2.4. PDE methods for minimization

Likewise for DW image denoising, the minima of (19) satisfy the Euler-Lagrange equation associated to the cost functional $V$ with Neumann boundary conditions:

$$\frac{\partial H(G)}{\partial G} + \lambda \frac{\partial \Phi(G)}{\partial G} = 0 \tag{23}$$

where

$$\begin{aligned}
\frac{\partial H_{\mathrm{Gauss}}(G)}{\partial G} &= \nabla H_{\mathrm{Gauss}}(G) = -2b \sum_{i=1}^{N} \left[ (S_i(G) - \hat{S}_i) \times \frac{\partial S_i(G)}{\partial G} \right], \\
\frac{\partial H_{\mathrm{Rice}}(G)}{\partial G} &= \nabla H_{\mathrm{Rice}}(G) = -\frac{1}{\sigma^2} \sum_{i=1}^{N} \left[ \left( S_i(G) - \hat{S}_i \frac{I_1}{I_0} \left( \frac{S_i \hat{S}_i}{\sigma^2} \right) \right) \times \frac{\partial S_i(G)}{\partial G} \right], \\
\frac{\partial \Phi(G)}{\partial G} &= \nabla \Phi(G) = -\mathrm{div}(\phi'(\|\nabla G\|) \|\nabla G\|).
\end{aligned} \tag{24}$$

Note that $G = T$ for Euclidean regularization, $G = F$ for Cholesky regularization and $G = L$ for Log-Euclidean regularization. The derivative $\partial S_i(L)/\partial L$ uses the directional derivative of the exponential $\partial_{g_i g_i^{\mathrm{t}}} \exp(L)$ that is detailed in Fillard et al. (2007).

Again, to avoid the difficult direct resolution of these PDE, we use the standard gradient descent technique. Starting from an initial function $G^0$, the iterative evolution of gradient descent is given by

$$G^{l+1} = G^l - \alpha^l \nabla V(G) \tag{25}$$

where $\nabla V(G) = \nabla H(G) + \lambda \nabla \Phi(G)$ is the gradient of $V$, $\alpha^l$ is the gradient descent step associated with the $l$-th iterate that satisfies Wolfe's conditions and the initial function $G^0$ is the classical least-squares estimation (where non-positive tensors are replaced by the mean of positive neighbours in the case of Log-Euclidean and Cholesky regularization).

Note that specific attention must be paid to the positive definiteness of the tensors. For Euclidean regularization, there is a risk of stepping out from the tensor space for each displacement $\alpha^l \nabla V(G)$. An idea is to project, after each iteration, the tensor $G^{l+1}$ on the underlying tensor space (this process is only used for Euclidean regularization, since positivity is ensured for Cholesky and Log-Euclidean regularization). More sophisticated approaches have been proposed in order to avoid this post-processing projection step. For instance, Chefd'hotel et al. (2004) propose a differential-geometric framework to deal with PDE flows lying directly on tensor space.

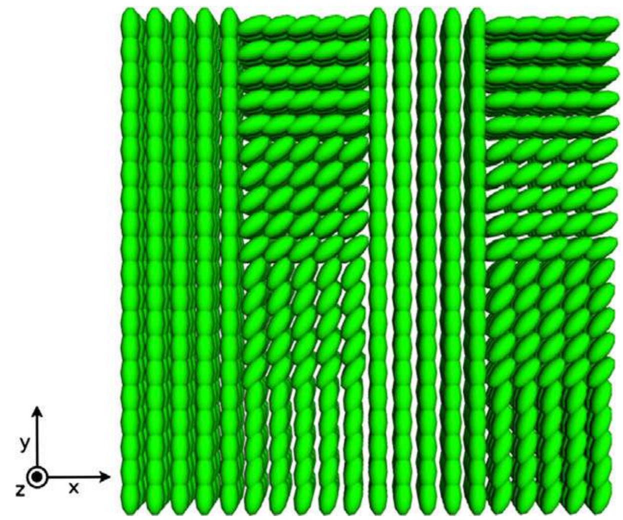


**Fig. 1.** Tensor field associated with synthetic data.

## 3. Experimental setup

### 3.1. Synthetic data

A diffusion tensor, $T$, is a $3 \times 3$ symmetric, positive definite matrix which can be decomposed as follows:

$$T = \begin{pmatrix} T_{xx} & T_{xy} & T_{xz} \\ T_{xy} & T_{yy} & T_{yz} \\ T_{xz} & T_{yz} & T_{zz} \end{pmatrix} = R \begin{pmatrix} \lambda_1 & 0 & 0 \\ 0 & \lambda_2 & 0 \\ 0 & 0 & \lambda_3 \end{pmatrix} R^{\mathrm{t}}, \tag{26}$$

where $\lambda_1, \lambda_2, \lambda_3$ are the eigenvalues of $T$ and $R$ is an orthogonal matrix.

We generated a $20 \times 20 \times 20$ artificial tensor field with 10 different homogeneous regions separated by discontinuities of different amplitudes (see Fig. 1).

Each $z$-slice of the tensor field is defined by the following matrix:

$$\begin{pmatrix} R_0 & R_1 & R_0 & R_2 \\ R_0 & R_3 & R_0 & R_4 \\ R_0 & R_5 & R_0 & R_6 \\ R_0 & R_7 & R_0 & R_8 \end{pmatrix}, \tag{27}$$

where each $R_i$ represents a $5 \times 5$ homogeneous tensor region, whose tensor coefficients are given in Table 1.

We used the Stejskal-Tanner diffusion equations to compute the DW images from this artificial tensor field. The associated $S_0$ image was chosen to be constant and we considered the cuboctahedron encoding scheme (six directions) to simulate the gradient sequence. Rician noise was added to the ideal DW images

**Table 1**
Tensor coefficients defining the synthetic dataset.

| $T$ | $T_{xx}$ | $T_{yy}$ | $T_{zz}$ | $T_{xy}$ | $T_{xz}$ | $T_{yz}$ |
|---|---|---|---|---|---|---|
| $R_0$ | 1 | 2 | 1 | 0 | 0 | 0 |
| $R_1$ | 1.04 | 1.96 | 1 | 0.19 | 0 | 0 |
| $R_2$ | 1.14 | 1.86 | 1 | 0.35 | 0 | 0 |
| $R_3$ | 1.3 | 1.70 | 1 | 0.46 | 0 | 0 |
| $R_4$ | 1.48 | 1.52 | 1 | 0.5 | 0 | 0 |
| $R_5$ | 1.67 | 1.33 | 1 | 0.47 | 0 | 0 |
| $R_6$ | 1.83 | 1.17 | 1 | 0.37 | 0 | 0 |
| $R_7$ | 1.95 | 1.05 | 1 | 0.22 | 0 | 0 |
| $R_8$ | 1.99 | 1.001 | 1 | 0 | 0 | 0 |

(Gudbjartsson and Patz, 1995) for different standard deviation values: $\sigma = 0.02$ (PSNR $\simeq$ 22 dB), $\sigma = 0.05$ (PSNR $\simeq$ 9 dB) and $\sigma = 0.1$ (PSNR $\simeq$ 4 dB). Given a discrete volume $f$ and its noisy representation $d$, the PSNR (peak signal-to-noise ratio) is defined by

$$\mathrm{PSNR} = 10 \cdot \log_{10}\left(\frac{\Delta f^2}{\frac{1}{N_V}\|d - f\|_2^2}\right), \tag{28}$$

where $\Delta f$ is the voxel value range, $\|\cdot\|_2$ is the standard Euclidean norm and $N_V$ is the number of voxels.

The resulting series of noisy DW images were used to estimate a discrete DT field using a standard least-squares estimation. Fig. 2 shows example of simulated DW images together with the corresponding synthetic DT fields. Regularization methods operate either on synthetic noisy DW images or synthetic noisy DT field, depending on the class they belong to.

### 3.2. Real data acquisition

In vivo heart acquisitions are very experimental and quite difficult to obtain. Our real data comes from a set of sixteen ex vivo human hearts. Ex vivo hearts have the benefit to be static, enabling large acquisition time without suffering from artefacts due to cardiac and respiratory motions. Nevertheless, since these hearts are processed a few hours after death our data is similar to data acquired in the in vivo context (in the case $(N_d, N_e) = (12, 1)$). For the most part, the cardiac fibre architecture is preserved.

The hearts were not perfused with any fixing agent in order not to change their diffusion properties. Care was taken to fix hearts in the same cardiac phase so that their fibre orientations would be similar. However, small variations in cardiac phase during fixation are not problematic since fibre angles do not change significantly between diastole and systole. Each heart was placed in a plastic container filled with the perfluoropolyether Fomblin (the low dielectric effect and minimal MR signal of Fomblin increases contrast and eliminates unwanted susceptibility artifacts near the boundaries of the heart).

The data were acquired with a Siemens Avanto 1.5T MR Scanner, using echo planar acquisitions. Each DW volume consists of 52 contiguous axial slices of size $128 \times 128$ (the spatial resolution is $2 \times 2 \times 2$ mm$^3$). We considered four different acquisition protocols defined by the number $N_d$ of diffusion sensitizing directions and the number $N_e$ of excitations used for signal averaging: $(N_d, N_e) = (12, 1), (12, 4), (12, 8)$ and $(12, 32)$ as illustrated in Fig. 3. Note that the truncated octahedron configuration was used for these protocols.

A large panel of acquisition protocols were analysed and compared in Frindel et al. (2007). The protocol $(N_d, N_e) = (12, 4)$ was chosen as the reference, because it gave the best results in terms of fibre direction coherence. The reference protocol used here for the evaluation of the regularization methods was acquired with the same number of directions but a much higher number of excitations (i.e. $N_e = 32$). In fact, scanning the ex vivo hearts for a long time enables the SNR to get really high, so that one can assume that almost no noise remains. The acquisition time and PSNR value (the DW volume of the protocol $(12, 32)$ plays the role of $f$) associated with each protocol are given in Table 2.

### 3.3. Evaluation methods

For suitable comparison, each regularization method is run with the values of the hyper-parameters $\lambda$ and $\delta$ that produce the best solution in terms of the mean Frobenius distance to the "ideal" tensor field (i.e. the standard least-squares estimation computed from the noiseless DW images in the case of synthetic data, and the standard least-squares estimation computed from the DW images of the reference protocol in the case of real data). The optimal sets of hyper-parameters were estimated from the solutions given by the different regularization methods at each point of a regular 2-D grid in the hyper-parameter space. The comparison of the best solutions from the different regularization methods was performed at each major step of the DT-MRI processing pipeline: tensor field representation, parametric maps and fibre tracking.

#### 3.3.1. Tensor field

In the case of tensor field representation, we compared the mean Frobenius distance between the regularized DT field and:

- the original noiseless DT field in the case of synthetic data,
- the reference protocol DT field in the case of real data.

Also note that in the case of real data a mask was applied to the DT field in order to compare only the tensors related to the myocardium. The segmentation was performed by selecting the voxels

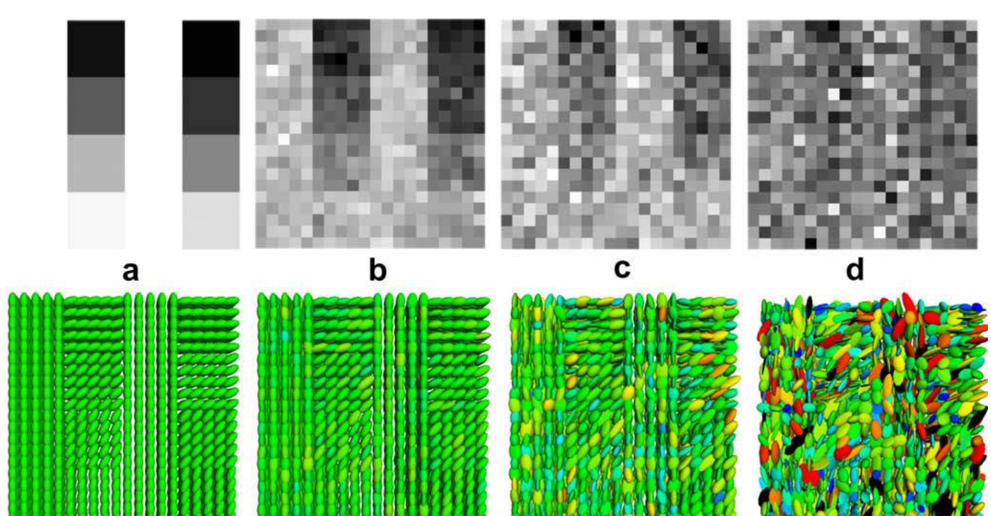


**Fig. 2.** Simulated DW image examples and associated DT fields (standard least-squares estimation) with: (a) no noise, (b) $\sigma = 0.02$, (c) $\sigma = 0.05$ and (d) $\sigma = 0.1$. The encoding gradient related to the DW image is $G = 1/\sqrt{2}(1, 0, 1)$.

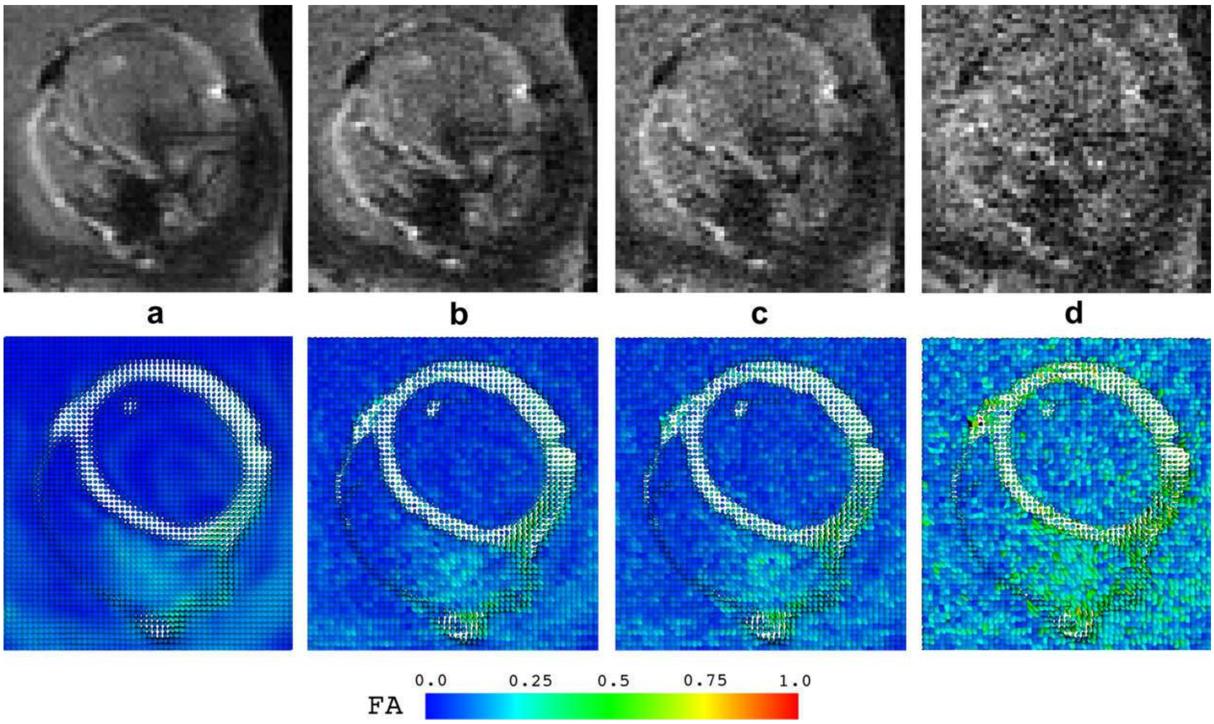


**Fig. 3.** Real cardiac DW images and corresponding DT fields (standard least-squares estimation) associated with $(N_d, N_e)$: (a) (12,32), (b) (12,8), (c) (12,4) and (d) (12,1). The encoding gradient associated with the DW image is $G = (1.0, 0, 0.5)$. It allows observation of the swelling effect caused by noise on tensors and how these phenomena lead to an overestimation of fractional anisotropy.

**Table 2**
Acquisition time and PSNR value associated with each protocol.

| Protocol $(N_d, N_e)$ | Time (min:sec) | PSNR (dB) |
|---|---|---|
| (12,1) | 2:02 | 10.02 |
| (12,4) | 7:37 | 16.44 |
| (12,8) | 15:09 | 20.09 |
| (12,32) | 63:93 | Ref. |

in the reference DW volume whose intensity belongs to the characteristic intensity range of muscles in T2 weighted MRI, as exemplified by Fig. 4.

#### 3.3.2. Parametric maps

When considering parametric maps, we compared the sum of the $\ell_1$-norm of the difference between the parametric maps computed from the regularized DT field and:

- the parametric maps associated with the noiseless DT field in the case of synthetic data,
- the parametric maps associated with the reference protocol in the case of real data (using the myocardium mask described above).

The parametric indices used in this study are mean diffusivity (MD), fractional anisotropy (FA) and coherence index (CI). Each of

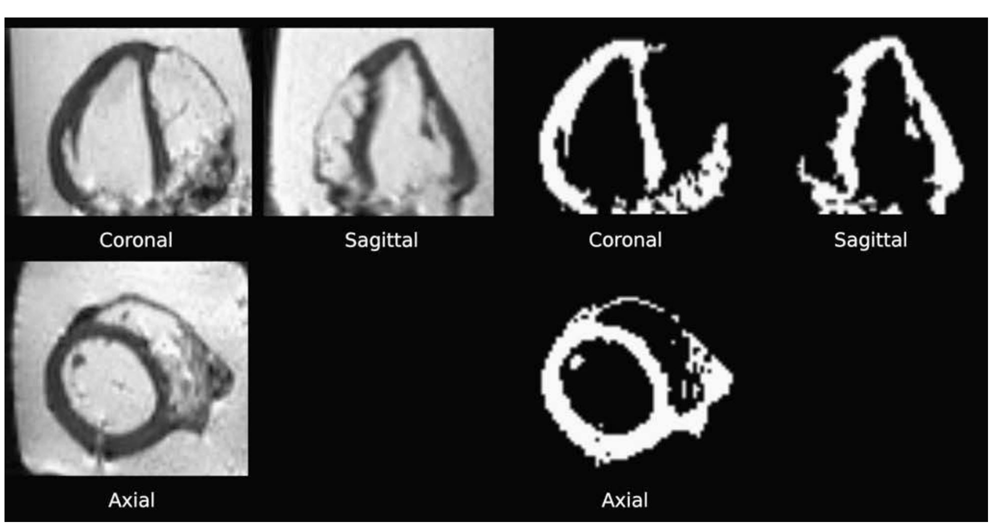


**Fig. 4.** Human heart segmentation. Left: T2 weighted MRI slices. Right: Mask after thresholding on the corresponding T2 weighted images.

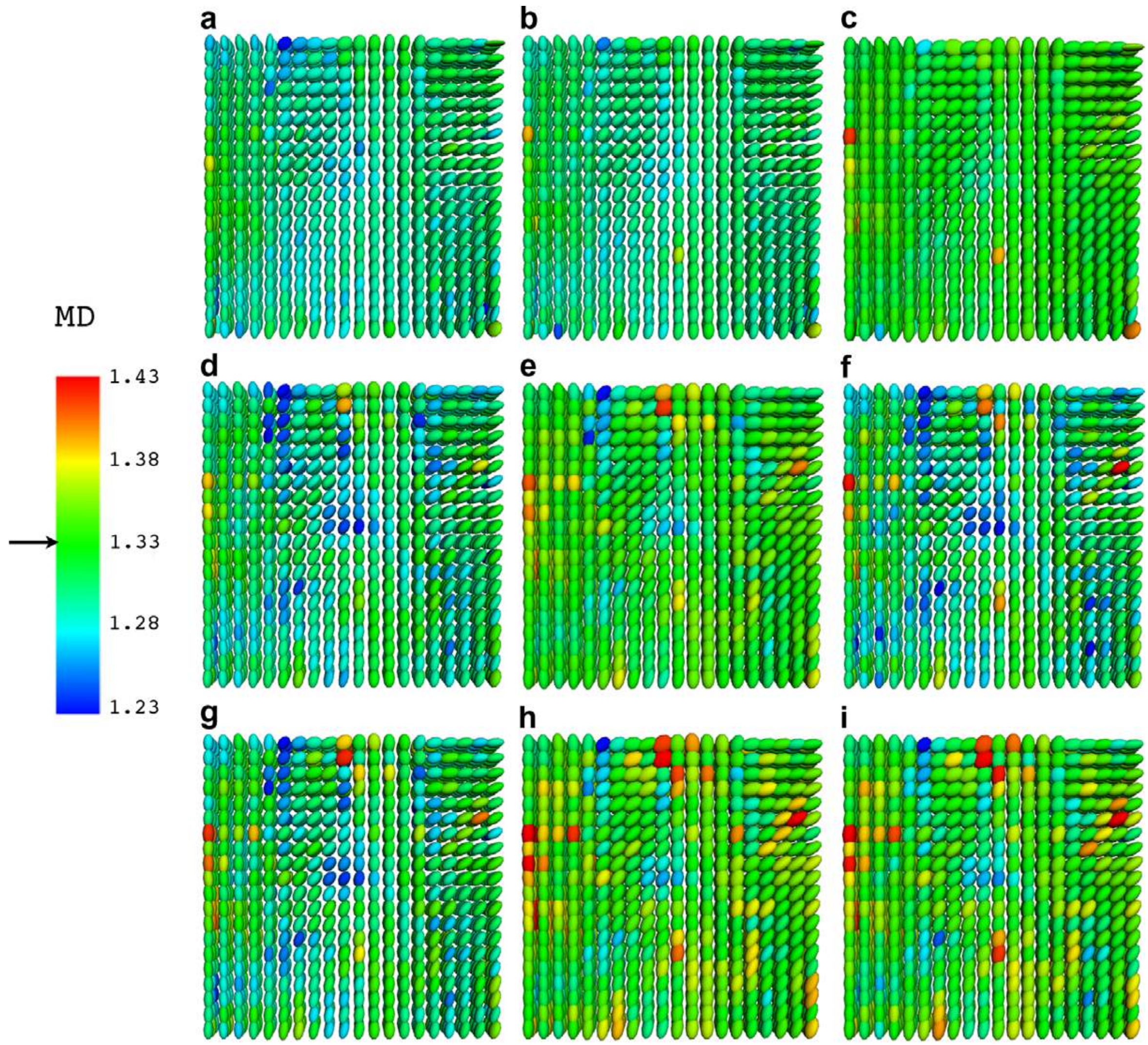


**Fig. 5.** DT field estimations mapped with mean diffusivity values ($\sigma = 0.1$). The arrow indicates the MD value of the noiseless synthetic dataset. (a) Weighted TV-norm regularization ($\lambda = 0.017$). (b) Gaussian anisotropic diffusion ($\lambda = 3e-4$, $\delta = 0.01$). (c) Rician anisotropic regularization ($\lambda = 3e-4, \delta = 0.01$). (d) Gaussian euclidian regularization ($\lambda = 0.7, \delta = 0.05$). (e) Rician euclidian regularization ($\lambda = 0.7, \delta = 0.05$). (f) Gaussian cholesky regularization ($\lambda = 0.65, \delta = 0.05$). (g) Gaussian Log-Euclidean regularization ($\lambda = 0.21, \delta = 0.05$). (h) Rician Log-Euclidean regularization ($\lambda = 0.21, \delta = 0.05$). (i): Rician cholesky regularization ($\lambda = 0.65, \delta = 0.05$).

them gives a different piece of information about local water diffusion: FA (Kingsley, 2006) measures deviation from isotropy and reflects the degree of alignment of cellular structures within fibre tracts, MD (Kingsley, 2006) measures average molecular motion, and CI (Basser and Pierpaoli, 1996) estimates the smoothness of the principal diffusion direction field.

For real datasets, we also considered the fibre helix angle $\alpha$ (Scollan et al., 1998) and the heart sheet angle $\beta$ (Tseng et al., 2003). These indices are commonly used to analyze the heart architecture; they enable comparison of DT-MRI measurements with the structure known from histological studies.

## 4. Results

### 4.1. Synthetic data

We applied the methods described in Section 2 on a synthetic dataset, which was corrupted by three different levels of noise ($\sigma = 0.02$, $\sigma = 0.05$ and $\sigma = 0.1$). In order to compare the methods quantitatively, we computed the mean Frobenius, FA, CI and MD errors (per voxel). Results are summarized in Table 3.

Let us first focus on the metric operating on tensors (the first column of Table 3): we find out that the method giving the best solution depends on the noise level. For $\sigma = 0.02$, the methods operating on DW images perform significant better than those working on tensors in terms of Frobenius error. Gaussian and Rician noise models do not make much difference on estimation quality. Therefore, in this situation, the SNR is high enough to approximate the effective Rician noise distribution by a Gaussian distribution (Sijbers et al., 1998). For $\sigma = 0.05$, the difference between regularization methods working on DW images and DT fields is less significant. However, the mean Frobenius error indicates that Rician regularization methods provide better estimations than Gaussian ones. Because of this significant difference, we conclude that above this value of $\sigma$, the SNR becomes too low to approximate the effective Rician noise distribution by a Gaussian distribution. Finally for $\sigma = 0.1$, Rician Log-Euclidean and Cholesky regularization methods perform significantly better than others in terms of Frobenius error. This suggests that when the SNR is too low, constraints to preserve tensor properties and coupling between tensor components improve the estimation of tensor fields.

The effects of regularization on parametric maps are detailed in the last three columns of Table 3. It is necessary to look at these

**Table 3**
Mean errors associated with estimations from synthetic datasets.

| | Method | Frobenius distance | CI | FA | MD |
|---|---|---|---|---|---|
| $\sigma = 0.02$ | | | | | |
| DWI regularization | Least-squares estimation | 0.201 | 0.008 | 0.035 | 0.032 |
| | Weighted TV-norm regularization | 0.087 | 0.007 | 0.018 | 0.008 |
| | Gauss anisotropic diffusion | 0.088 | 0.008 | 0.018 | 0.010 |
| | Rice anisotropic diffusion | 0.086 | 0.008 | 0.016 | 0.008 |
| DT regularization | Gauss euclidian regularization | 0.102 | 0.008 | 0.019 | 0.013 |
| | Rice euclidian regularization | 0.101 | 0.008 | 0.019 | 0.013 |
| | Gauss Log-Euclidean regularization | 0.110 | 0.010 | 0.020 | 0.015 |
| | Rice Log-Euclidean regularization | 0.108 | 0.010 | 0.020 | 0.015 |
| | Gauss cholesky regularization | 0.113 | 0.009 | 0.021 | 0.017 |
| | Rice cholesky regularization | 0.112 | 0.009 | 0.021 | 0.017 |
| $\sigma = 0.05$ | | | | | |
| DWI regularization | Least-squares estimation | 0.506 | 0.057 | 0.081 | 0.081 |
| | Weighted TV-norm regularization | 0.166 | 0.014 | 0.031 | 0.020 |
| | Gauss anisotropic diffusion | 0.191 | 0.016 | 0.038 | 0.019 |
| | Rice anisotropic diffusion | 0.162 | 0.009 | 0.029 | 0.014 |
| DT regularization | Gauss euclidian regularization | 0.189 | 0.014 | 0.031 | 0.033 |
| | Rice euclidian regularization | 0.173 | 0.013 | 0.030 | 0.021 |
| | Gauss Log-Euclidean regularization | 0.173 | 0.014 | 0.030 | 0.030 |
| | Rice Log-Euclidean regularization | 0.160 | 0.013 | 0.028 | 0.019 |
| | Gauss cholesky regularization | 0.183 | 0.016 | 0.030 | 0.034 |
| | Rician cholesky regularization | 0.168 | 0.015 | 0.029 | 0.022 |
| $\sigma = 0.1$ | | | | | |
| DWI regularization | Least-squares estimation | 1.127 | 0.253 | 0.184 | 0.183 |
| | Weighted TV-norm regularization | 0.270 | 0.020 | 0.060 | 0.042 |
| | Gauss anisotropic diffusion | 0.294 | 0.024 | 0.072 | 0.053 |
| | Rice anisotropic diffusion | 0.285 | 0.022 | 0.061 | 0.020 |
| DT regularization | Gauss euclidian regularization | 0.300 | 0.022 | 0.068 | 0.052 |
| | Rice euclidian regularization | 0.267 | 0.018 | 0.059 | 0.034 |
| | Gauss Log-Euclidean regularization | 0.272 | 0.021 | 0.063 | 0.055 |
| | Rice Log-Euclidean regularization | 0.247 | 0.016 | 0.052 | 0.038 |
| | Gauss cholesky regularization | 0.293 | 0.025 | 0.067 | 0.061 |
| | Rice cholesky regularization | 0.256 | 0.019 | 0.056 | 0.043 |

maps in order to characterize the different regularization methods in terms of diffusion properties recovery. We notice that FA increases with noise for standard least-squares estimations as reported in previous work (Basu et al., 2006; Skare et al., 2000). Concerning the regularization methods, we notice that if the SNR is low, the Log-Euclidean DT-regularization method is less sensitive to noise in terms of FA. It preserves the anisotropic shape of the tensor while the other methods tend to produce more isotropic tensors. As pointed out in (Arsigny et al., 2005), the Log-Euclidean metric preserves tensor volumes more accurately than the Euclidean metric does (the latter often leading to overestimation of the diffusion). Fig. 6 illustrates this contrast between Log-Euclidean and the other regularization methods.

Conversely, MD is underestimated when noise increases, which is a direct consequence of approximating the Rician noise distribution by a Gaussian distribution. In fact, when the SNR is high ($\sigma = 0.02$), the different regularization methods have almost the same characteristics in terms of MD. But when the SNR is low ($\sigma = 0.1$), the Rician noise model inhibit the tensor shrinking effect observed with the Gaussian noise model. This phenomenon has been mentioned in Fillard et al. (2007) and lies in the fact that the magnitude of DW signal appears to be greater than it really is, resulting in the estimations of tensors whose diffusivity tends to be smaller then it actually is (a higher signal magnitude means a lower diffusion). This phenomenon is particularly visible in Fig. 5.

These experiments revealed two important facts about the two classes of regularization methods studied here. On the one hand, when the SNR is high, the methods giving the best results in terms of estimation are those operating directly on DW images. This implies that working at the early stage of DW images has the benefit of reducing the magnitude of noise-based errors propagated through diffusion calculations. On the other hand, when the SNR is low, the Rician regularization methods preserving the tensor's properties (Log-Euclidean framework) and respecting the noise characteristics (Rician model), give the best results in terms of estimation and tensor direction alignment.

### 4.2. Real data

We applied the methods described in Section 2 on real datasets acquired with acquisition protocols of various quality: $(N_d, N_e) = (12, 32), (12, 8), (12, 4)$ and $(12,1)$. The acquisition protocol (12,32) served as a reference and enabled us to validate the estimations obtained from the data associated with the other protocols. To evaluate estimations quality, we compute the mean error (per voxel) associated to the Frobenius norm on the tensor field and to the $\ell_1$-norm for CI, FA, MD, $\alpha$ and $\beta$ maps. This evaluation is only performed within the myocardium region, which is segmented with a mask (Section 3.3.1). Results are summarized in Table 4.

First, we noticed that the results obtained from real datasets are coherent with those associated with synthetic datasets. However, the difference between the regularization methods tends to be globally less significant, which can be explained by the relatively high PNSR of the protocols $(N_d, N_e) = (12, 8), (12, 4)$ and $(12,1)$ w.r.t. the reference protocol (12,32). The regularization methods giving the best estimations for the data acquired from the protocol ($N_d$, $N_e$) = (12,8) (PSNR $\simeq$ 20.09 dB) are the ones working on DW images and there is no significant difference between the Rician and Gaussian noise models. By contrast, in the case of data acquired from the protocol ($N_d$, $N_e$) = (12,1) (PSNR $\simeq$ 10.02 dB), the

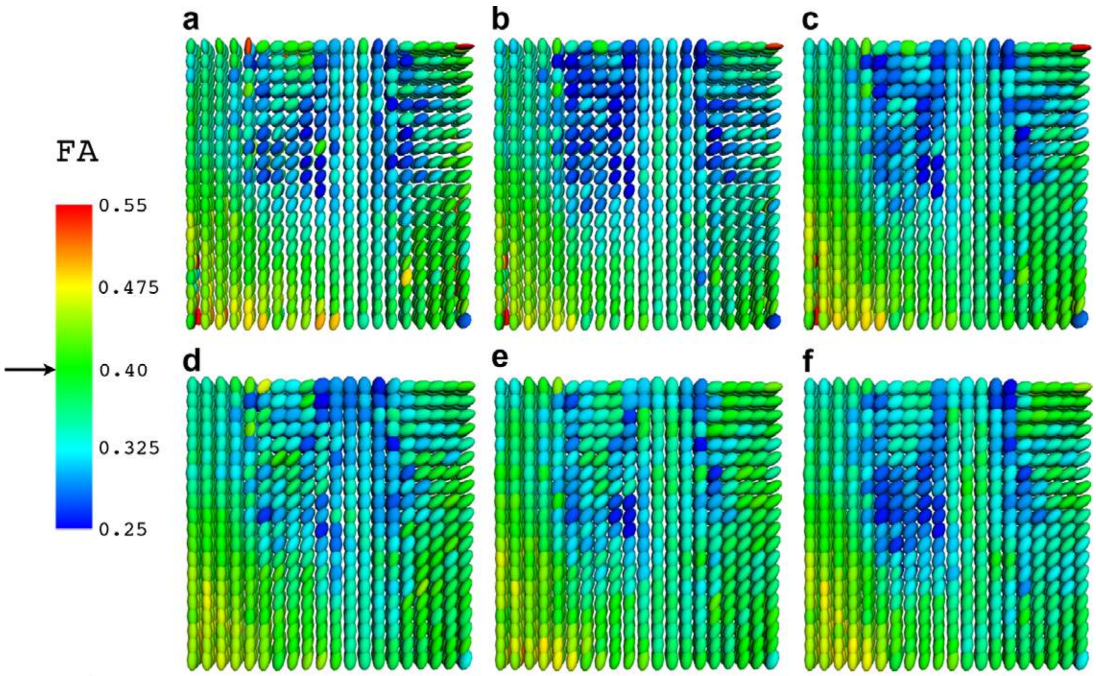


**Fig. 6.** DT field estimations mapped with fractional anisotropy values ($\sigma = 0.1$). The arrow indicates FA of the noiseless synthetic dataset. (a) Weighted TV-norm regularization. (b) Gaussian anisotropic diffusion. (c) Rician anisotropic regularization. (d) Rician euclidian regularization. (e) Rician Log-Euclidean regularization. (f) Rician cholesky regularization.

**Table 4**
Mean errors associated with estimations from a real cardiac dataset.

| | Method | Frobenius distance | CI | FA | MD | $\alpha$ (°) | $\beta$ (°) |
|---|---|---|---|---|---|---|---|
| $(N_d, N_e) = (12, 8)$ | | | | | | | |
| DWI regularization | Least-squares estimation | 0.293 | 0.221 | 0.079 | 0.126 | 27.86 | 15.64 |
| | Weighted TV-norm regularization | 0.101 | 0.047 | 0.004 | 0.062 | 11.75 | 9.01 |
| | Gauss anisotropic diffusion | 0.102 | 0.047 | 0.004 | 0.065 | 11.81 | 9.10 |
| | Rice anisotropic diffusion | 0.099 | 0.046 | 0.003 | 0.062 | 11.61 | 8.91 |
| DT regularization | Gauss euclidian regularization | 0.116 | 0.054 | 0.007 | 0.068 | 12.97 | 9.38 |
| | Rice euclidian regularization | 0.114 | 0.053 | 0.007 | 0.068 | 11.64 | 9.19 |
| | Gauss Log-Euclidean regularization | 0.124 | 0.056 | 0.009 | 0.069 | 12.06 | 9.47 |
| | Rice Log-Euclidean regularization | 0.122 | 0.054 | 0.009 | 0.068 | 11.69 | 9.25 |
| | Gauss cholesky regularization | 0.125 | 0.057 | 0.010 | 0.070 | 12.18 | 9.67 |
| | Rice cholesky regularization | 0.122 | 0.055 | 0.009 | 0.069 | 11.83 | 9.38 |
| $(N_d, N_e) = (12, 4)$ | | | | | | | |
| DWI regularization | Least-squares estimation | 0.341 | 0.291 | 0.099 | 0.129 | 31.56 | 19.22 |
| | W. TV-norm regularization | 0.121 | 0.064 | 0.013 | 0.089 | 15.84 | 11.14 |
| | Gauss anisotropic diffusion | 0.128 | 0.071 | 0.017 | 0.091 | 15.86 | 11.46 |
| | Rice anisotropic diffusion | 0.119 | 0.068 | 0.015 | 0.085 | 15.12 | 9.84 |
| DT regularization | Gauss euclidian regularization | 0.132 | 0.071 | 0.018 | 0.091 | 16.12 | 11.70 |
| | Rice euclidian regularization | 0.128 | 0.066 | 0.016 | 0.084 | 15.56 | 10.83 |
| | Gauss Log-Euclidean regularization | 0.127 | 0.065 | 0.015 | 0.087 | 15.95 | 11.72 |
| | Rice Log-Euclidean regularization | 0.120 | 0.059 | 0.012 | 0.079 | 15.44 | 10.98 |
| | Gauss cholesky regularization | 0.129 | 0.069 | 0.017 | 0.089 | 15.99 | 11.63 |
| | Rician cholesky regularization | 0.122 | 0.063 | 0.014 | 0.083 | 15.62 | 10.95 |
| $(N_d, N_e) = (12, 1)$ | | | | | | | |
| DWI regularization | Least-squares estimation | 0.559 | 0.373 | 0.248 | 0.142 | 34.52 | 17.41 |
| | Weighted TV-norm regularization | 0.215 | 0.101 | 0.043 | 0.092 | 18.65 | 11.47 |
| | Gauss anisotropic diffusion | 0.233 | 0.134 | 0.055 | 0.095 | 19.36 | 12.41 |
| | Rice anisotropic diffusion | 0.210 | 0.114 | 0.051 | 0.074 | 16.55 | 10.62 |
| DT regularization | Gauss euclidian regularization | 0.216 | 0.121 | 0.057 | 0.072 | 20.20 | 12.64 |
| | Rice euclidian regularization | 0.198 | 0.107 | 0.053 | 0.054 | 19.45 | 11.29 |
| | Gauss Log-Euclidean regularization | 0.171 | 0.102 | 0.036 | 0.068 | 20.47 | 12.48 |
| | Rice Log-Euclidean regularization | 0.149 | 0.099 | 0.032 | 0.042 | 19.86 | 11.22 |
| | Gauss cholesky regularization | 0.179 | 0.108 | 0.038 | 0.069 | 19.86 | 13.37 |
| | Rice cholesky regularization | 0.152 | 0.103 | 0.033 | 0.046 | 18.68 | 12.15 |

regularization methods operating on tensor fields with constraints on tensor symmetry and positive definiteness produced the best results. In addition, the difference between the Rician and the Gaussian noise models is significant, which emphasizes that the approximation of the Rician noise distribution by a Gaussian distribution leads to errors that cannot be tolerated.

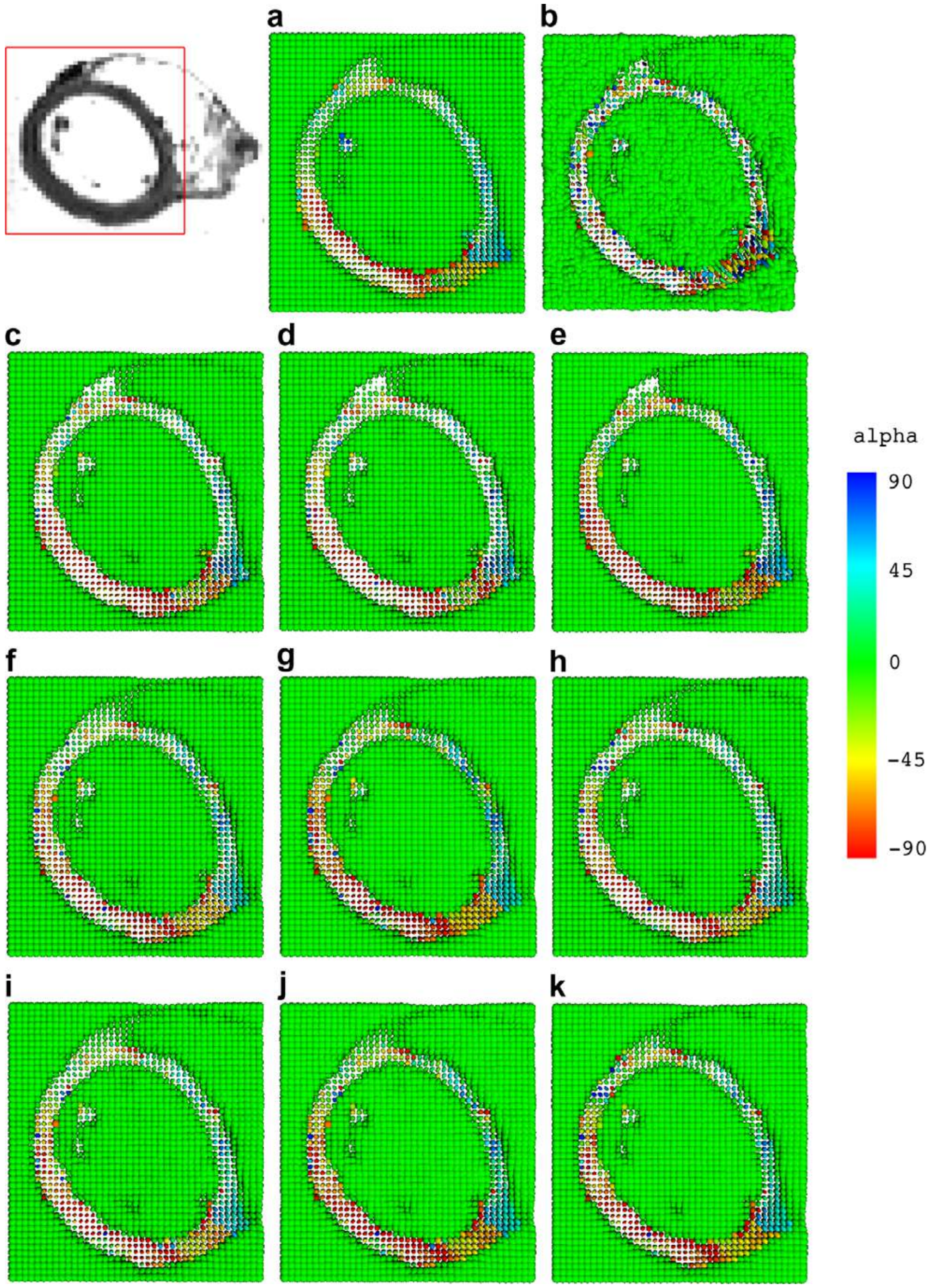


**Fig. 7.** Regularization results on a real dataset acquired with the protocol $(N_d, N_e) = (12, 1)$. The figures are a close up of the region delimited by the red square and are mapped using the helix angle $\alpha$. (a) (12,32) reference dataset. (b) (12,1) dataset. (c) Weighted TV-norm regularization ($\lambda = 13$). (d) Gaussian anisotropic diffusion ($\lambda = 22, \delta = 1$). (e) Rician anisotropic diffusion ($\lambda = 22, \delta = 1, \sigma = 4$). (f) Gaussian euclidian regularization ($\lambda = 0.6, \delta = 0.05$). (g) Rician euclidian regularization ($\lambda = 0.6, \delta = 0.05, \sigma = 4$). (h) Gaussian Log-Euclidean regularization ($\lambda = 0.15, \delta = 0.05$). (i) Gaussian cholesky regularization ($\lambda = 0.54, \delta = 0.05$). (j) Rician cholesky regularization ($\lambda = 0.54, \delta = 0.05, \sigma = 4$). (k) Rician Log-Euclidean regularization ($\lambda = 0.15, \delta = 0.05, \sigma = 4$).

Second, the effects of regularization on the parametric maps FA, MD and CI lead to the same conclusions as those obtained with synthetic datasets. When the SNR is low, i.e. $(N_d, N_e) = (12, 1)$, Cholesky and Log-Euclidean regularization methods give the best results in terms of the degree of alignment within the fibre tracts (FA). However, in isotropic regions like the ones containing the gel, the nearby anisotropic regions have an influence on the regularization process: tensors located on the boundaries are corrupted by small anisotropic ones (Fig. 8). Now, considering average molecular motion (MD), in the low SNR case, the use of the Rician noise model produces better results than the Gaussian model: it leads to estimated tensors that are not squeezed and that are closer to the reference tensors computed from the data associated with the reference protocol (Fig. 7).

Third, the effects of regularization on structural index maps (helix and sheet angles, $\alpha$ and $\beta$) are detailed in the last two columns of Table 4. When $(N_d, N_e) = (12, 8)$, the mean Frobenius, FA and MD errors are consistent with the fact that the regularization methods working on DW images provide better estimations. They allow more likely measurement of global diffusion than methods working on tensor fields. The helix and sheet angles agree with these observations. On the other hand, when $(N_d, N_e) = (12, 1)$, Rician

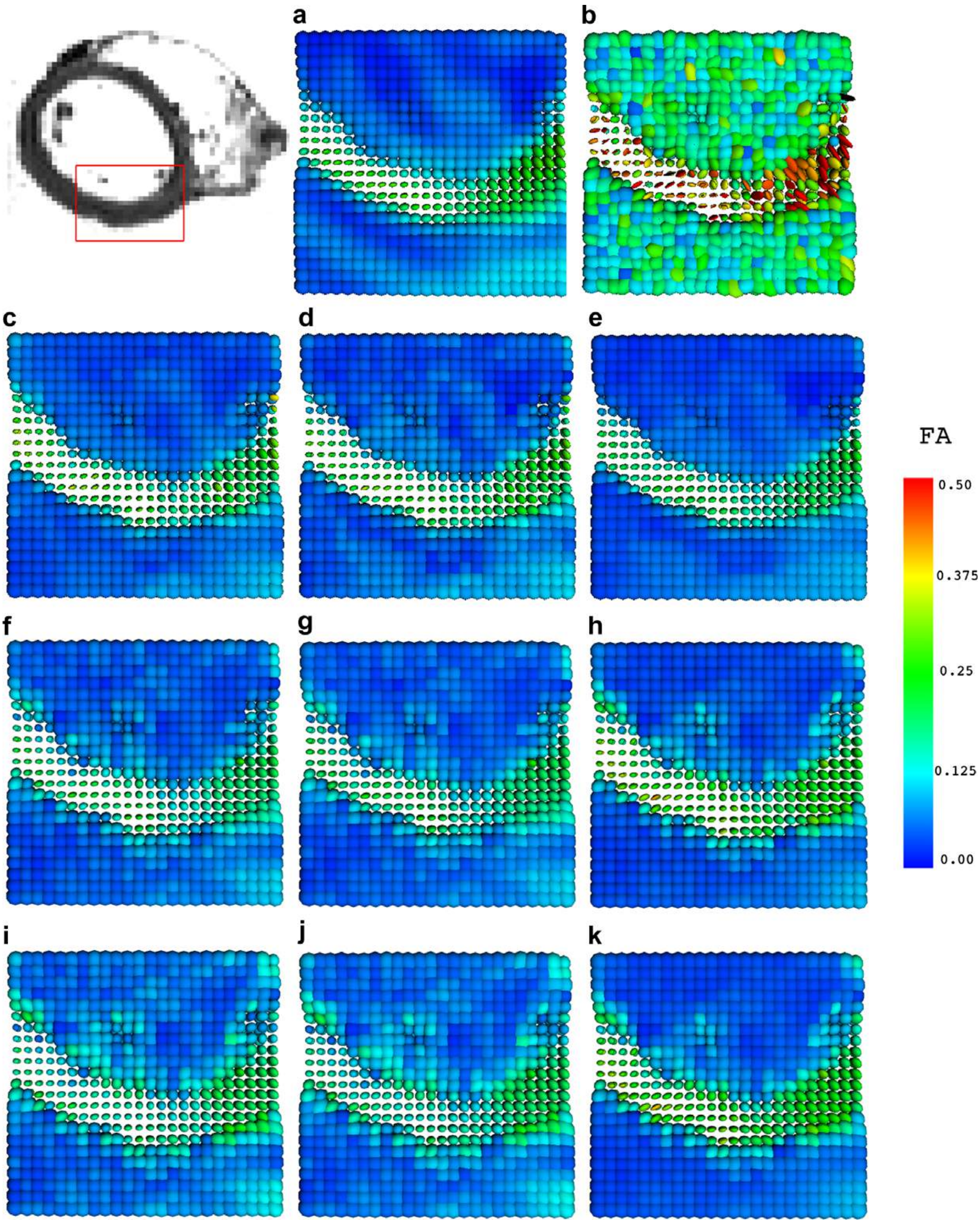


**Fig. 8.** Regularization results on a real dataset acquired with the protocol $(N_d, N_e) = (12, 1)$. The figures are a close up of the region delimited by the red square and are mapped using fractional anisotropy. (a) (12,32) reference dataset. (b) (12,1) dataset. (c) Weighted TV-norm regularization. (d) Gaussian anisotropic diffusion. (e) Rician anisotropic diffusion. (f) Gaussian euclidian regularization. (g) Rician euclidian regularization. (h) Gaussian Log-Euclidean regularization. (i) Gaussian cholesky regularization. (j) Rician cholesky regularization. (k) Rician Log-Euclidean regularization.

regularization methods provide the best results in terms of the structural angles $\alpha$ and $\beta$. Preventing the tensor shrinking phenomenon improves the diffusivity measurement, which has a direct impact on the estimation of the human heart architecture. Finally, note that regularization methods preserving tensor properties (Log-Euclidean and Cholesky frameworks) do not present better results than the methods that work on DW images.

### 4.3. Tractography

Tractography or fibre extraction, is a process that takes place at the very end of the DT-MRI processing pipeline and requires a smooth principal diffusion direction field to ensure the reliability of fibre extraction. Among the methods for tracking fibres, we chose streamlining tractography (Basser et al., 2000) and show

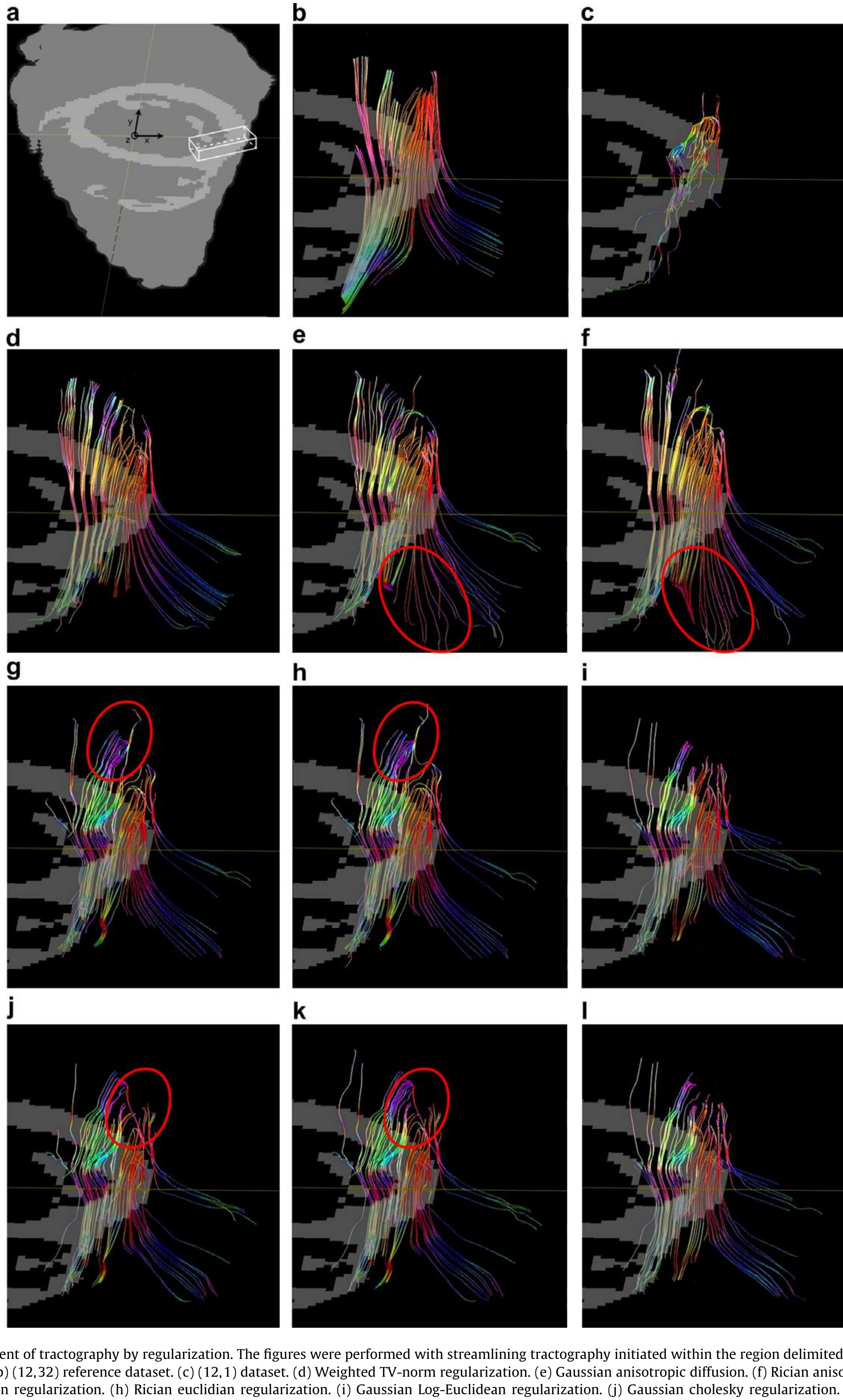


**Fig. 9.** Improvement of tractography by regularization. The figures were performed with streamlining tractography initiated within the region delimited by the gray square. (a) Seed region. (b) (12, 32) reference dataset. (c) (12, 1) dataset. (d) Weighted TV-norm regularization. (e) Gaussian anisotropic diffusion. (f) Rician anisotropic diffusion. (g) Gaussian euclidian regularization. (h) Rician euclidian regularization. (i) Gaussian Log-Euclidean regularization. (j) Gaussian cholesky regularization. (k) Rician cholesky regularization. (l) Rician Log-Euclidean regularization.

how the tracking can be improved by the regularization methods under investigation. The criteria for stopping the tracking are: a threshold on FA (tracking is stopped when FA is too small) and on the curvature (to forbid highly bended fibres that do not match the cardiac architecture). We tracked the fibres from the tensor fields obtained by standard least-squares estimation from the regularized DW images or by the DT regularization estimations. The parameters used for tracking are, 0.05 for the FA threshold and 20° for the maximum angle of deviation threshold.

Tracking results corresponding to the protocol $(N_d, N_e) = (12, 1)$ across the left ventricular wall are shown in Fig. 9. The figure is obtained by launching trajectories from a multislice region of interest (ROI) of $10 \times 3 \times 3$ voxels in the body of the left ventricle. We require the fractional anisotropy index of all voxels within the ROI to be greater than 0.35 to ensure that the fibre tracts are launched from regions of coherently organized cardiac bundles with no partial volume effect. On one hand, the reference protocol (12,32) emphasizes the helical structure within the left ventricle: it shows that the extracted fibres rotate clockwise from the apex to the base in the epicardium, have circular geometry in the midwall, and rotate counterclockwise in the endocardium. On the other hand, the protocol (12,1) presents fuzzy and very short fibres, which can be explained by the high noise level. Using regularization, the tracking is qualitatively much smoother than the one performed on the tensor field estimated from protocol (12,1) raw data. Smoothing the tensor field or the DW images leads to more regular and longer fibres, that are closer to those computed directly from the reference protocol (12,32).

We performed one final analysis to compare the different regularization methods w.r.t. the helical structure characterizing the heart architecture. As summarized in Table 5, we computed the following criteria for each tractography result: (i) the number $N_f$ of fibres which length ranges between 20 and 100 mm, (ii) the volume $V_f$ defined by the voxels crossed by the predicted fibres, (ii) the mean fibre length $\mu_{fl}$, (iv) the coefficient of fibre length variation (CV), which is defined as the ratio of the fibre length standard deviation $\sigma_{fl}$ to the mean $\mu_{fl}$ and (v) the percentage of matching points in the regularized fibres trajectories and the fibre trajectories estimated from the reference protocol. Globally, the shape of the fibre tracts does not differ much from one regularization method to another. However, the Rician noise model leads to larger values of $V_f$ and $N_f$ and to a better matching score: tracts that were stopped or dispersed due to noise error propagation are now fully reconstructed. Note that best matching score is attributed to DW images regularization methods. Nevertheless, the difference with DT-regularization methods is not significant, which can be explained by the relative high PSNR of our real data.

Finally, let us make some qualitative observations about the results depicted in Fig. 9. First, one can observe a difference between weighted TV-norm regularization and classical anisotropic diffusion. The emphasized regions for Rician and Gaussian anisotropic diffusion (Fig. 9e and f) are artefactual (in the sense that they do not appear in the reference fibre bundle). Conversely, the weighted TV-norm regularization method – allowing synchronization of the evolution of the DW images (based on anisotropy) – helps to better distinguish which information is reliable for fibre tracking. Second, one can observe a difference between the Log-Euclidean regularization method and the other DT-regularization methods. The emphasized regions for Euclidean and Cholesky regularization methods (Fig. 9g–k) are also artefactual. As discussed in Sections 4.1 and 4.2, the Log-Euclidean metric preserves tensor volumes more accurately than does the Euclidean metric (the latter often leads to overestimation of the diffusion). The Euclidean metric, by it swelling effect, increases fractional anisotropy and thus leads to longer fibres. However this does not mean that fibres are correct, as shown in Fig. 9.

## 5. Conclusions

In this paper, we presented an comprehensive comparison of DW images and DT field regularization methods, in the context of DT-MR imaging of the human ex vivo heart. We considered two noise models for each approach: either we assume that the data are corrupted by Rician noise and estimation is achieved by means of a maximum likelihood technique adapted to the nature of noise, or we assume that the noise is Gaussian and estimation is achieved by means of standard least-squares estimation. These estimators are combined with an anisotropic regularization term operating on the DW images or on the DT field. These computing frameworks are substantially different from one another, and thus there is a need to establish which is more adapted to a particular situation.

Results on synthetic data show that, below a PSNR value of 9 dB, the Rician maximum likelihood estimator limits the shrinking effect, while the Gaussian noise model leads to a loss of tensor volumes (mean diffusivity is underestimated). Concerning the contrast between DW image and DT field based regularization approaches, we notice that above a PNSR value of approximately 9 dB the methods operating on DW images produce cleaner data and thus prevent noise error propagation through the diffusion calculations. Conversely, below a PSNR value of 9 dB, the Cholesky and the Log-Euclidean frameworks overcome the limitations of standard Euclidean calculus: in that they guarantee the symmetry and positive definiteness of the tensors.

In order to evaluate the results from the real data quantitatively, we used the reference protocol studied in Frindel et al. (2007). Results from real data of reasonable quality (PSNR ranging between 10 and 20 dB w.r.t. the reference protocol, depending on $N_e$ and $N_d$) are consistent with those obtained with synthetic data, though less significant. For protocols (12,8) and (12,4), the meth-

**Table 5**
Quantification on fibre tracts.

| | Method | $N_f$ | $V_f$ | $\mu_{fl}$ | $CV_{fl}$ | % Match |
|---|---|---|---|---|---|---|
| $(N_d, N_e) = (12, 32)$ | Least-squares estimation | 84 | 1113 | 21.91 | 0.56 | 100 |
| $(N_d, N_e) = (12, 1)$ | Least-squares estimation | 21 | 275 | 15.75 | 0.61 | 9.88 |
| DWI regularization | Weighted TV-norm regularization | 80 | 1192 | 19.93 | 0.49 | 49.51 |
| | Gauss anisotropic diffusion | 77 | 1173 | 18.63 | 0.46 | 44.77 |
| | Rice anisotropic diffusion | 82 | 1240 | 20.60 | 0.44 | 47.99 |
| DT regularization | Gauss euclidian regularization | 65 | 854 | 18.34 | 0.63 | 39.11 |
| | Rice euclidian regularization | 67 | 890 | 19.90 | 0.61 | 42.86 |
| | Gauss Log-Euclidean regularization | 62 | 800 | 18.13 | 0.62 | 40.98 |
| | Rice Log-Euclidean regularization | 68 | 849 | 19.63 | 0.59 | 44.81 |
| | Gauss cholesky regularization | 70 | 928 | 18.26 | 0.62 | 39.98 |
| | Rice cholesky regularization | 73 | 945 | 19.88 | 0.59 | 43.51 |

ods operating on DW images provide better estimation of the water diffusion. By contrast, with the low quality protocol (12, 1), we notice that the choice of the noise model is important to prevent underestimation of tensor volumes and that Cholesky and Log-Euclidean regularization methods better preserve tensor geometry (FA, MD and CI). From a qualitative point of view, the choice of the Rician noise model can be justified by the fact that it leads to fibre tracts that are smoother and more focused (w.r.t. the reference fibre bundle) than with the Gaussian noise model. It is however difficult to establish a qualitative difference between DW images and DT field regularization methods. Some fibre termination artefacts suggest that multivalued regularization approaches with specific constraints on tensor geometry are preferable (weighted TV-norm and Log-Euclidean regularization). Yet the differences are small enough to conclude that the quality of our DT-MRI data is sufficient to consider all regularization methods as equivalent.

## Acknowledgement

This work was supported by Siemens and the French ANRT. We would like to thank E. Stephant and S. Rapacchi for their help to acquire the DT-MRI data and also J. Dardenne for the development of the visualization tool.

## References

Arsigny, V., Fillard, P., Pennec, X., Ayache, N., 2005. Fast and simple calculus on tensors in the Log-Euclidean framework. In: MICCAI'2005, vol. 3749. pp. 115–122.

Basser, P.J., Pierpaoli, C., 1996. Microstructural and physiological features of tissues elucidated by quantitative-diffusion-tensor MRI. Journal of Magnetic Resonance, Series B 111 (3), 209–219.

Basser, P.J., Pajevic, S., Pierpaoli, C., Duda, J., Aldroubi, A., 2000. In vivo fiber tractography using DT-MRI data. Magnetic Resonance in Medicine 44 (4), 625–632.

Basu, S., Fletcher, P.T., Whitaker, R.T., 2006. Rician noise removal in diffusion tensor MRI. In: MICCAI'2006, vol. 4190. pp. 117–125.

Charbonnier, P., Blanc-Féraud, L., Aubert, G., Barlaud, M., 1997. Deterministic edge-preserving regularization in computed imaging. IEEE Transactions on Image Processing 6 (2), 298–311.

Chefd'hotel, C., Tschumperlé, D., Deriche, R., Faugeras, O., 2004. Regularizing flows for constrained matrix-valued images. Journal of Mathematical Imaging and Vision 20 (1–2), 147–162.

Deriche, R., Faugeras, O., 1996. Les EDP en traitement des images et vision par ordinateur. Traitement du Signal 13 (6).

Fillard, P., Arsigny, V., Pennec, X., Ayache, N., 2007. Clinical DT-MRI estimation, smoothing and fiber tracking with Log-Euclidean metrics. IEEE Transactions on Medical Imaging 26 (11), 1472–1482.

Frindel, C., Robini, M., Rapacchi, S., Stephant, E., Zhu, Y., Croisille, P., 2007. Towards in vivo diffusion tensor MRI on human heart using edge-preserving regularization. In: International Conference on IEEE EMBS'2007. pp. 6007–6010.

Gudbjartsson, H., Patz, S., 1995. The rician distribution of noisy MRI data. Magnetic Resonance in Medicine 36 (2), 910–914.

Henkelman, R.M., 1985. Measurement of signal intensities in the presence of noise in MR images. Medical Physics 12 (2), 232–233.

Kingsley, P.B., 2006. Introduction to diffusion tensor imaging mathematics: Part ii. anisotropy, diffusion-weighting factors, and gradient encoding schemes. Concepts in Magnetic Resonance Part A 28A (2), 123–154.

McGraw, T., Vemuri, B.C., Chen, Y., Rao, M., Mareci, T., 2004. DT-MRI de- noising and neuronal fiber tracking. Medical Image Analysis 8 (2), 95–111.

Parker, G.J.M., Schnabel, J.A., Symms, M.R., Werring, D.J., Barker, G.J., 2000. Nonlinear smoothing for reduction of systematic and random errors in diffusion tensor imaging. Magnetic Resonance in Medicine 11, 702–710.

Pennec, X., Fillard, P., Ayache, N., 2006. A Riemannian framework for tensor computing. International Journal of Computer Vision 66 (1), 41–66.

Perona, P., Malik, J., 1990. Scale-space and edge detection using anisotropic diffusion. IEEE Transactions on Pattern Analatycal Machine Intelligence 12, 629–639.

Peyrat, J.-M., Sermesant, M., Pennec, X., Delingette, H., Xu, C., McVeigh, E.R., Ayache, N., 2007. A computational framework for the statistical analysis of cardiac diffusion tensors: Application to a small database of canine hearts. IEEE Transactions on Medical Imaging, 1500–1514.

Rudin, L., Osher, S., Fatemi, E., 1992. Nonlinear total variation based noise removal algorithms. Physica D 60, 259–268.

Scollan, D.F., Holmes, A., Winslow, R.L., Forder, J., 1998. Histological validation of myocardial microstructure obtained from diffusion tensor magnetic resonance imaging. American Journal of Physiology – Heart Circulatory Physiology 275, H2308–H2318.

Sijbers, J., den Dekker, A.J., Van Audekerke, J., Verhoye, M., Van Dy-cket, D., 1998. Estimation of the noise in magnitude MR images. Medical Resonance Imaging 16 (1), 87–90.

Skare, S., Li, T.Q., Nordell, B., Ingvar, M., 2000. Noise considerations in the determination of diffusion tensor anisotropy. Magnetic Resonance Imaging 18, 659–669.

Tschumperle, D., Deriche, R., 2001. Diffusion tensor regularization with constraints preservation. In: International Conference on IEEE CVPR'2001, pp. 948–953.

Tseng, W.Y., Wedeen, V.J., Reese, T.G., Smith, R.N., Halpern, E.F., 2003. Diffusion tensor MRI of myocardial fibers and sheets: correspondence with visible cut-face texture. Magnetic Resonance in Medicine 17, 31–42.

Vemuri, B.C., Chen, Y., Rao, M., McGraw, T., Mareci, Z.T., 2001. Fiber tract mapping from diffusion tensor MRI. In: International Conference on IEEE VLSM'2001, pp. 81–88.

Wang, Z., Vemuri, B.C., Chen, Y., Mareci, T.H., 2004. A constrained variational principle for direct estimation and smoothing of the diffusion tensor field from complex DWI. IEEE Transactions on Medical Imaging 23 (8), 930–939.

Weickert, J., Brox, T., 2002. Diffusion and regularization of vector- and matrix-valued images. Inverse Problems, Image Analysis, and Medical Imaging 313, 251–268.

Wolfe, P., 1969. Convergence conditions for ascent methods. SIAM Review 11, 226–235.

Wolfe, P., 1971. Convergence conditions for ascent methods (ii): some corrections. SIAM Review 13, 185–188.

You, Y.L., Xu, W., Tannenbaum, A., Kaveh, M., 1996. Behavioral analysis of anisotropic diffusion in image processing. IEEE Transactions on Image Processing 5, 1539–1553.